The Simultaneous Measurement of Reversed Phase-Encoding EPI in a Single fMRI Session: Evaluation of Geometric Distortion Correction in Submillimetre fMRI at 7T

Seong Dae Yun, PhD[1*], Erhan Genc[2], Jeongbeen Lee[1,3], and N. Jon Shah, PhD[1,4,5,6]

[1]Institute of Neuroscience and Medicine 4, INM-4, Forschungszentrum Jülich, Jülich, Germany

[2]Department of Psychology and Neurosciences, Leibniz Research Centre for Working Environment and Human Factors (IfADo), Dortmund, Germany

[3]Department of Brain and Cognitive Sciences, Scranton College, Ewha Womans University, Seoul, Republic of Korea

[4]Institute of Neuroscience and Medicine 11, INM-11, JARA, Forschungszentrum Jülich, Jülich, Germany

[5]JARA - BRAIN - Translational Medicine, Aachen, Germany

[6]Department of Neurology, RWTH Aachen University, Aachen, Germany

To whom correspondence may be addressed:

Dr. Seong Dae Yun*

Institute of Neuroscience and Medicine 4, Forschungszentrum Jülich, 52425 Jülich, Germany

Tel: +49 2461 61 2085,

Email: s.yun@fz-juelich.de

ORCID: https://orcid.org/0000-0001-7398-1899

Abstract

The high temporal resolution of echo-planar imaging (EPI) has driven its widespread use in functional MRI (fMRI), and recent advancements in EPI have enabled the mapping of cortical layer-specific functional activities. Notwithstanding these technical innovations, geometric distortion correction in EPI remains essential to ensure accurate functional mapping onto anatomical references. A common approach for distortion correction involves the acquisition of an additional scan, with the phase-encoding direction reversed. However, this extra scan necessitates redundant acquisitions of calibration scans, significantly increasing acquisition time and energy deposition. To address this concern, this work presents a novel EPI scheme that simultaneously acquires both the original and reversed phase-encoding data within a single fMRI session. Furthermore, despite the widespread use of distortion correction, methods for qualitative and quantitative evaluation of its impact on submillimetre fMRI analysis have remained largely unexplored. This study acquires submillimetre visual fMRI data (0.73×0.73 mm^2) at 7T using the suggested EPI scheme and evaluates the impact of distortion correction through various metrics proposed here, including spatial resolution, co-registration accuracy, functional mapping fidelity, and distribution of functional voxels. Our fMRI acquisition scheme effectively reduced redundant acquisition time and total energy deposition to subjects. Distortion-corrected fMRI data demonstrated significant improvements in co-registration with anatomical scans, thereby enhancing functional mapping accuracy. The improvements were achieved without significant degradation of spatial resolution or alteration of the functional activation distribution. These findings were verified through qualitative and quantitative assessments, highlighting the effectiveness of distortion correction in submillimetre fMRI.

Keywords

Blip-up-blip-down, Co-registration, Distortion correction, EPI, fMRI, Functional mapping accuracy, and Submillimetre resolution.

Highlights

- We present a novel fMRI scheme that effectively acquires reversed-PE EPI data
- Our fMRI scheme substantially reduces extra acquisition time and energy deposition
- The impact of EPI distortion correction is evaluated for submillimetre fMRI
- We propose diverse qualitative and quantitative metrics, enabling thorough analysis
- Distortion correction demonstrates its effectiveness for high-fidelity fMRI mapping

1. Introduction

The advent of echo-planar imaging (EPI) (Mansfield, 1977) has facilitated the development of various dynamic MRI applications. Its relatively high temporal resolution makes it particularly well-suited for detecting time-dependent variation in signal contrast, leading to its widespread use in applications such as diffusion and functional MRI (fMRI) studies. Recent advancements in EPI techniques and associated image analysis methods have now enabled the characterisation of physiological quantities in the brain with respect to the cortical depths, providing deeper insights into brain function and clinical abnormalities.

Despite these technical innovations, the relatively low receiver bandwidth along the phase-encoding (PE) direction in EPI significantly contributes to the development of geometric deformation of tissue structures, making image analysis based on accurate anatomical references challenging. This geometric distortion can be effectively mitigated through technical approaches such as improved shimming (Balteau et al., 2010; Kim et al., 2016) or readout-acceleration techniques, including parallel imaging, partial Fourier, or multi-shot methods. However, they may necessitate technically more demanding configurations, especially when operating at higher field strengths or aiming for higher-resolution imaging with an increased readout length.

Alternatively, a widely adopted methodological approach to address the EPI distortion is the direct unwarping of geometric distortions using an additional EPI scan acquired with the reversed PE direction (Chang and Fitzpatrick, 1992; Morgan et al., 2004), commonly referred to as the ‘blip-up-blip-down’ method. This approach exploits the fact that distortions in the reversed PE data develop toward the opposite direction, enabling the data-driven calculation and relocation of voxel shifts between the two different PE directions without prior knowledge of the B_0 offset (Jezzard and Balaban, 1995; Chen and Wyrwicz, 1999;

Hutton et al., 2002) or PSF (Robson et al., 1997; Zeng and Constable 2002; Zaitsev et al., 2004; Chung et al., 2011; Patzig et al., 2021). Moreover, the reversed PE data can be obtained using the same sequence, indicating that no additional sequence implementation is required, unlike the B_0 and PSF methods. Several comparative studies have demonstrated the superior performance of the blip-up-blip-down method over the B_0 field map method (Wang et al., 2017; Malekian et al., 2023).

However, one concern that has not been extensively explored in the blip-up-blip-down method is the potential increase in redundant acquisition time and specific absorption ratio (SAR) accrued during the acquisition of reversed-PE EPI. This arises due to the fact that the reversed PE data are typically acquired by adding an extra run of the same EPI protocol, only with the change in the PE direction, resulting in a repeated measurement of calibration scans for image reconstruction. To address this issue, this work presents a novel EPI scheme that additionally acquires EPI data with the reversed PE direction within a single fMRI session, thereby facilitating the analysis of distortion-corrected images with reduced motion effects. This proposed scheme is expected to shorten the total acquisition time while reducing energy deposition, particularly for fMRI, which requires a large imaging matrix size to achieve high spatial resolution and whole-brain coverage.

In addition, notwithstanding the widespread use of the blip-up-blip-down method for the analysis of submillimetre fMRI data (Kashyap et al., 2018; Marquardt et al., 2018; Jia et al., 2020; Huang et al., 2021; Navarro et al., 2021; Schellekens et al., 2023; Yun et al., 2023), the evaluation of the distortion-correction performance and its potential impact on fMRI data has remained largely unexplored in the context of the submillimetre fMRI. While several previous studies have demonstrated the effectiveness of distortion correction (Hutton et al., 2002; Dymerska et al., 2018; Duong et al., 2020; Patzig et al., 2021; Montez et al., 2023), most have primarily focused on structural improvements in distortion-corrected EPI and its

co-registration accuracy with anatomical scans, often overlooking the impact of distortion correction on high-resolution functional data.

Another objective of this work is to propose quantitative and qualitative metrics for the comprehensive evaluation of the performance of distortion-corrected fMRI data in terms of structural and functional mapping quality. This includes the assessment of potential spatial resolution degradation, which is crucial for submillimetre fMRI analysis, the examination of structural alignment between functional and anatomical scans, and the evaluation of functional mapping accuracy along with a statistical comparison of activated voxels. This study validates the feasibility of the proposed fMRI scheme and the performance evaluation metrics using submillimetre (0.73×0.73 mm^2) fMRI data acquired on a 7T MRI scanner.

2. Materials and Methods

2.1. Study subject and ethics statement

All in vivo measurements were performed on healthy volunteers who underwent standard safety screening procedures. None had any medical conditions or suffered from any neurological or psychiatric illnesses. After receiving a complete explanation of the study, all participants provided written informed consent before scanning. The study protocol, screening questionnaires, and consent forms were approved by the local institutional review board at RWTH Aachen University, Germany (EK 346/17). Five healthy volunteers participated in this study, during which visual stimuli were applied.

2.2. Proposed EPI scheme

Figure 1a shows a schematic representation of a typical fMRI run using the standard EPI scheme, consisting of three stages: calibration, dummy, and actual fMRI scans. Before starting the actual fMRI scans, two preceding measurements, namely calibration and dummy scans, are performed, which are necessary for the reconstruction of acceleration techniques and for reaching a steady state (Yun et al., 2023). The acquisition of calibration data is assumed to be included here, as most high-resolution fMRI protocols commonly employ acceleration techniques such as parallel imaging. In the standard scheme, EPI with reversed PE is typically performed by adding a second run of the same protocol, differing only in the PE direction; see the blue and red arrows indicating the PE directions in the fMRI and reversed PE measurements, respectively. This approach suggests that the second session still requires another complete acquisition of the calibration data, although the reversed-PE EPI data only need to be reconstructed for a few temporal volumes.

While the fMRI scan is acquired using EPI, the calibration scan for the parallel imaging is often acquired using sequences more tolerant to field inhomogeneities, such as a conventional line-by-line excitation, spoiled gradient-recalled (SPGR) sequence, ensuring more robust kernel calibration at ultra-high fields. However, the SPGR scheme requires a relatively long acquisition time, making the repeated acquisition of the calibration scan in the standard scheme increasingly redundant. To resolve this issue, the proposed scheme acquires the first two dummy scans– excluded from image analysis– using reversed PE, while the remaining scans are acquired with the original PE directions (Yun et al., 2023). This strategy allows a single calibration kernel to be shared to reconstruct both the original and reversed-PE EPI data, effectively reducing the total acquisition time and SAR for parallel imaging calibration. In this work, the number of dummy and reversed PE scans was set to four and two, respectively, as illustrated in the figure.

2.3. Imaging protocols: submillimetre visual fMRI

A visual checkerboard paradigm was employed for in vivo fMRI experiments to elicit circumscribed activation in the visual cortex (Yun et al., 2013, 2017). The passive viewing task involved a simple block design in which a black and white checkerboard, reversing at a frequency of 8 Hz, alternated with low-level baseline phases (fixation cross). The paradigm consisted of four dummy scans for reaching a steady state, followed by 96 scans comprising eight cycles of baseline-activation states. Each cycle lasted six volume acquisitions, resulting in a total duration of 21 seconds. As described in the previous section, the first two dummy scans were acquired with the reversed PE direction.

The feasibility of using the proposed EPI scheme for visual fMRI was verified with the following imaging parameters: TR/TE = 3500/22 ms, FOV (AP × LR × FH) = 210 × 210 × 117 mm3, matrix = 288 × 288 with 117 axial slices

(0.73 × 0.73 × 1.0 mm3), flip angle = 90°, partial Fourier = 5/8, parallel imaging = 3-fold, multi-band = three-fold, and receiver bandwidth = 965 Hz/Px. The parallel imaging calibration data were acquired using the SPGR sequence with an auto-calibration signal (ACS) size of 72. For the assessment of reversed PE data from the proposed scheme, additional reversed PE data were separately acquired using the standard scheme (see Fig. 1b). A 3D anatomical image was acquired using a T1-weighted magnetisation-prepared, rapid gradient echo (MP2RAGE) sequence with the following configuration: TR/TE/TI1/TI2 = 4440/2.08/840/2370 ms, FOV (FH × AP × LR) = 240 × 226 × 154 mm3, matrix size = 400 × 376 with 256 sagittal slices (0.6 mm isotropic), flip angles = 5°/6°, parallel imaging = 3-fold, and receiver bandwidth = 250 Hz/Px. The above imaging setup was implemented on a Siemens Magnetom Terra 7T scanner with a single-channel Tx and 32-channel Rx Nova medical coil supplied by the manufacturer.

2.4. Distortion correction: blip-up-blip-down method

Geometric distortion in the original fMRI time-series data (96 temporal volumes) was corrected using reversed-PE data (two temporal volumes in the dummy can) acquired from the proposed scheme. This blip-up-blip-down method was implemented using a publicly available image processing toolkit, Advanced Normalization Tools (ANTs) (https://github.com/srikash; https://github.com/ANTsX/ANTs; Avants et al., 2010; Esteban et al., 2019; Tustison et al., 2021). ANTs computes the warping field of the original EPI data while simultaneously estimating subject motion displacements, enabling correction of both motion and distortion within the time series in a single interpolation step. This strategy assists in minimising potential spatial resolution degradation, which may be more pronounced when motion and distortion are corrected separately (Glasser et al., 2013; Wang et al., 2022).

To validate the use of reversed-PE data from the proposed scheme, the same ANTs correction process was repeated using reversed-PE data acquired with the standard scheme in a separate session (see Fig. 1a). Differences in motion displacement between the proposed and standard schemes were examined, and their impact on distortion correction was assessed.

2.5. Performance evaluation: qualitative and quantitative metrics

2.5.1. Spatial resolution

It has been previously reported that the distortion correction step involves resampling of voxels or sub-voxel shifts, which can result in a loss of effective spatial resolution (Renvall et al., 2016; Kashyap et al., 2018; Polimeni et el., 2018; Wang et al., 2022). This study thoroughly investigates the potential degradation of spatial resolution caused by the unwarping process during distortion correction, building upon and modifying an approach proposed in previous work (Renvall et al., 2016).

The original EPI image was subjected to the standard spatial smoothing procedure in SPM12 (Wellcome Department of Imaging Neuroscience, UCL, London, UK; https://www.fil.ion.ucl.ac.uk/spm/software/spm12/) using Gaussian smoothing kernel widths (σ) ranging from 0.2 to 0.8 mm in 0.1 mm increment. A region-of-interest (ROI) was selected in the white matter (WM), where the signal variation in the region was relatively homogeneous. The standard deviation (SD) within the ROI was computed for the original and the smoothed EPI images, creating a lookup table to examine the spatial resolution based on the SD values. A lower SD indicated greater spatial resolution degradation due to more intensive Gaussian smoothing with a larger kernel size. The SD was then computed for the distortion-corrected EPI image and compared to the lookup table to identify the closest match. The corresponding smoothing kernel size was used to estimate the degree of the spatial

resolution degradation (σ_{deg}) in the distortion-corrected image, as defined by the following formula:

$$\sigma_{deg} = \arg\min_{\sigma} |SD_{corr} - SD_{\sigma}|, \sigma \in \{0.0, 0.2, 0.3, \ldots, 0.8\}\, mm \quad (1)$$

, where SD_{corr} and SD_{σ} represent the SD from the distortion-corrected image and the original EPI images smoothed with different kernel widths, respectively, with σ = 0.0 indicating no smoothing. σ_{deg} denotes the kernel width creating the closest match. For each fMRI data set, this computation was performed for every slice location, and the results were averaged across slices.

2.5.2. Structural similarity: co-registration

The original and distortion-corrected EPI images were independently co-registered to the MP2RAGE scan using the 'antsRegistrationSyN' module in the ANTs toolkit. In each case, the structural similarity between the EPI and the MP2RAGE scans was visually inspected by comparing the co-registered anatomical structures, particularly in regions like the frontal lobe where EPI distortion is most pronounced. The similarity was further quantified using the Learned Perceptual Image Patch Similarity (LPIPS) index, a perceptual metric that measures image similarity by computing deep feature distances across multiple layers of a pre-trained neural network (Zhang et al., 2018). LPIPS captures perceptual differences by comparing feature maps extracted from various convolutional layers and aggregating their distances. Compared to traditional similarity metrics, such as L2, Structural Similarity Index Measure (SSIM) (Wang et al., 2004), and Feature Similarity Index Measure (FSIM) (Zhang et al., 2011), LPIPS exhibits a significantly stronger correlation with human perceptual judgments, making it a more robust evaluation metric for image similarity. In this work, LPIPS was configured with the Visual Geometry Group (VGG) network, which has

been shown to outperform shallower, more lightweight architectures like SqueezeNet in terms of perceptual similarity (Zhang et al., 2018).

For this comparison, the standard segmentation routine in SPM12 was applied individually to the EPI and MP2RAGE scans, generating probability maps for grey matter (GM), WM, and cerebrospinal fluid (CSF) masks. The probability maps obtained were then used to compute the LPIPS index as shown in the formula below, where a lower value indicates higher image similarity:

$$LPIPS(EP_{ROI}, MP_{ROI}) = \frac{1}{L}\sum_{l=1}^{L}\|f_l(EP_{ROI}) - f_l(MP_{ROI})\|_2^2, \mathrm{ROI} \in \{\mathrm{GM}, \mathrm{WM}, \mathrm{CSF}\} \quad (2)$$

, where EP_{ROI} and MP_{ROI} represent the probability maps of EPI and MP2RAGE at the selected ROI, respectively. f_l denotes the deep feature map extracted from the l-th convolutional layer, and L is the total number of layers considered in the computation. The computation was applied for each slice, and the average score was obtained. This approach allows for the comparison of structural similarity between the EPI and MPRAGE scans, each having different contrasts (i.e. T_2^* and T_1). Prior to data processing, background noise in the MP2RAGE scan, which was generated by combining the two inversion images into a single unified image, was removed using an open-source script (https://github.com/JosePMarques/MP2RAGE-related-scripts).

2.5.3. Functional mapping

For the original and distortion-corrected fMRI data sets, the first-level analysis was performed separately using the generalised linear model in SPM12, and the functional results obtained with an uncorrected p-value < 0.001 were overlaid on their respectively co-registered MP2RAGE scan for visual inspection. From the total number of activated voxels, the proportion located within the GM, as defined by the MP2RAGE scan, was calculated. To

minimise false positives in this analysis, only activated voxels with t-values of five or greater were included (Lohmann et al., 2018):

$$r_{GM} = N_{GM}(t \geq 5)/N_{Total}(t \geq 5),\ \ r_{Non-GM} = 1 - r_{GM} \tag{3}$$

, where r_{GM} and $r_{Non\text{-}GM}$ represent the ratio of activated voxels within the GM and non-GM regions, respectively. The ratios were computed for the results obtained from both the original and distortion-corrected fMRI datasets, and putative differences were examined.

Lastly, the impact of the distortion correction on the functional activation was inspected by analysing the histogram distribution of the *t*-values for the activated voxels. The histogram results obtained from the original and distortion-corrected fMRI data were compared, and the degree of matching between the two cases was quantitatively measured by computing the Pearson correlation coefficient:

$$\rho_{HO,HC} = \frac{\sum_{i=1}^{N}(HO_i - \overline{HO})(HC_i - \overline{HC})}{\sqrt{\sum_{i=1}^{N}(HO_i - \overline{HO})^2}\sqrt{\sum_{i=1}^{N}(HC_i - \overline{HC})^2}} \tag{4}$$

, where HO_i and HC_i represent the values of the *i*-th bin in the original and distortion-corrected histograms, respectively. *N* denotes the number of bins in the histograms. The differences in t-value distribution before and after distortion correction were statistically assessed using the Kolmogorov-Smirnov (KS) test:

$$D = \mathrm{Sup}_x \left| F_{org}(x) - F_{corr}(x) \right| \tag{5}$$

, where $F_{org}(x)$ and $F_{corr}(x)$ represent the cumulative distribution function of the t-values from the original and distortion-corrected results. *D* is the KS statistic that reflects the degree of discrepancy between the two distributions, with values ranging from 0 to 1. The corresponding *p*-value was also computed.

3. Results

3.1. Distortion correction using the proposed scheme

Figure 2 shows the results of distortion correction for fMRI scans at four representative slice locations, with the first and second rows displaying images obtained from the reversed (1st scan) and original PE (5th scan) directions. The last row shows the corresponding distortion-corrected results, revealing no significant visible loss of spatial resolution at any of the displaced slice locations. This result also demonstrates the feasibility of using the proposed fMRI scheme in the distortion correction. The distortion-corrected results at entire slice locations can be found in the Supplementary File (see Supplementary Figure 1).

Figure 3a displays reversed PE images obtained from both the standard and proposed schemes at a representative slice location. Figure 3b highlights the ventricle boundaries extracted from the reversed-PE images from the standard (yellow), overlaid on those from the proposed (magenta) schemes. This image panel illustrates the significant motion displacement that occurred between the fMRI session and the subsequent session for acquiring reversed-PE data in the standard scheme. The corresponding distortion-corrected results, obtained using both reversed-PE images, are shown in Fig. 3c. Both methods effectively eliminate the geometric distortions present in the original EPI image (Fig. 3d). However, the proposed method demonstrates greater improvement in signal recovery around the frontal lobe, as well as the clearer delineation of the GM and WM boundaries (see the regions marked by arrows in Fig. 3e). Furthermore, the proposed simultaneous acquisition scheme significantly reduces the redundant SAR and acquisition time for the acquisition of reversed-PE EPI. A more detailed analysis, including the technical aspects of the imaging sequences, is presented in the supplementary Table 1.

3.2. Assessment of spatial resolution

Figure 4a displays the original and distortion-corrected EPI images at a representative slice location. The yellow ROIs indicate the region used for the SD computation in the quantitative assessment of spatial resolution. The rectangular ROIs mark the areas where spatial resolution was visually inspected, with an enlarged view provided in Fig. 4b. The enlarged views of the original image, outlined in white rectangular ROIs, illustrate the effects of various smoothing kernel widths, where a decrease in spatial resolution becomes more apparent at larger kernel widths. For the selected slice location, visual inspection of Fig. 4b suggests that the loss of spatial resolution induced by distortion correction was not significant.

Table 1 presents the obtained lookup table at the above slice location, listing the SD values of the original image and the spatially smoothed ones. The SD value of the corresponding distortion-corrected image was computed as 72.55, which is closest to that of the original image without smoothing. Consequently, the degree of the spatial resolution degradation (σ_{deg}) was determined to be 0.0. The results of σ_{deg} obtained at all slice locations are presented in the box-plot in Figure 5. The results from four out of five subjects show that the median value was zero, with the third quartile ranging between 0.2 and 0.3. While the third subject showed a relatively higher third quartile, the median value remained low at around 0.3. These findings suggest that the spatial resolution degradation caused by distortion correction was not significant.

3.3. Co-registration between the functional and anatomical scan

The EPI images, co-registered with the MP2RAGE scan, were transformed from the subject space to the anatomical space, and results from a representative subject are shown in Fig. 6. Both the EPI and MP2RAGE scans are presented in three sectional views (i.e. axial,

coronal and sagittal), each depicting the counterpart of the brain. That is, for the axial and coronal presentation, the EPI and MP2RAGE scans display the left and right hemispheres, whereas they show the upper and lower halves for the sagittal presentation, respectively.

To aid visual comparison, the contour of the ventricles (i.e. the lateral and fourth ventricles) obtained from the MP2RAGE scan are depicted in yellow. Here, improved alignments between the EPI and MP2RAGE scans are clearly observed in the distortion-corrected case (Fig. 6b) when compared to the original, uncorrected one (Fig. 6a); a substantial misalignment of the ventricles in the boundaries between the two scans can be found in the original EPI case. The aforementioned ventricle areas are extracted from the EPI images using signal thresholding, and the results from both the original EPI (red-yellow) and corrected EPI (blue-light blue) images are overlaid onto the MP2RAGE scan in Fig. 6c. This representation clearly illustrates the substantial improvements in co-registration achieved through distortion-correction. Specifically, in the sagittal presentation, the geometric deformations present in the frontal lobe of the original EPI image (i.e. shrunken structures) are demonstrated to be effectively reduced in the distortion-corrected case. As a result, the boundary between the cingulate gyrus and corpus callosum is also well aligned between the EPI and MP2RAGE scans, as indicated by the regions marked by red arrows.

Table 2 presents the results of the calculated LPIPS index obtained from the five-subject datasets. For all examined ROIs (GM, WM and CSF), a substantial reduction in the LPIPS index (i.e. greater similarity between the EPI and MP2RAGE scans) was observed in the distortion-corrected results when compared to original image across all subjects.

3.4. Analysis of fMRI data

Figure 7 displays activated voxels obtained from the original (red-white) and distortion-corrected (cyan-magenta) fMRI data sets, overlaid on the respective co-registered

MP2RAGE scan. Significant differences in the distribution of activated voxels are clearly visible between the original and distortion-corrected results (Fig. 7a). In separate representations of the original and distortion-corrected results (Figs. 7b and c), the distortion-corrected case demonstrates improved alignment of activated voxels within GM regions, whereas the original data show that the activated voxels are partially identified outside the GM regions. This is clearly seen in the enlarged representation of the selected rectangular ROIs (see yellow arrows). Table 3 presents the ratio of activated voxels located in the GM and non-GM regions (r_{GM} and $r_{Non\text{-}GM}$). A substantial increase in r_{GM} was observed in the distortion-corrected case when compared to the original, consistently across all five subjects. The mean ± SD of r_{GM} in the distortion-corrected case was 88.58 ± 2.51%, which was, on average, 8.33% higher than that of the original (80.25 ± 1.69%).

Figure 8 shows the histogram distribution of t-values obtained from the original and distortion-corrected fMRI data sets, presented in blue and orange, respectively. Visual inspection of the histogram distribution suggests that the original and distortion-corrected results exhibit highly similar features across all five subjects, implying that the distortion correction had no significant impact on the overall distribution of functional activation. Table 4 presents the computed correlation coefficients ($\rho_{HO,HC}$) and KS statistics (D and p-value) between the two distributions. For all subjects, $\rho_{HO,HC}$ exceed 0.99, and the p-value was greater than 0.05, with the D value being close to zero, indicating no statistically significant difference between the two distributions.

4. Discussion

This work proposes an EPI scheme that acquires both original and reversed PE-direction EPI in a single fMRI session and demonstrates its applicability for the distortion correction of submillimetre fMRI data at 7T. When compared to the standard scheme, the proposed approach effectively reduces additional acquisition time, RF energy accumulation, and subject motion accrued during the acquisition between the two different PE directions. This advantage becomes more prominent when the parallel imaging calibration scan is acquired using the SPGR sequence, a method commonly adopted at ultra-high fields for more robust calibration of the reconstruction kernel. In this study, the SPGR sequence was configured with 72 ACS lines, a relatively high number intended to enhance reconstructed image quality. Albeit at the cost of an increase in the scanning time, this approach serves as a straightforward solution unless more elaborated sampling methods (Park et al., 2005; Wang et al., 2014) or advanced kernel calibration techniques (Aja-Fernández et al., 2015; Sheng et al., 2021; Chang et al., 2022) are implemented. In this regime, the advantages of the proposed EPI become more pronounced, as it eliminates the need for repeated acquisition of the calibration scan, which would otherwise significantly prolong the acquisition in the standard scheme.

The geometric distortion in the original fMRI data was significantly reduced through the blip-up-blip-down method. While other distortion-correction techniques, such as the B_0-field map or PSF methods, have been previously demonstrated, a comparative assessment of various distortion-correction methods is not the focus of the current work, as this topic has already been explored in prior research (Zeng and Constable 2002; Wang et al., 2017; Patzig et al., 2021; Malekian et al., 2023). This study primarily focuses on a thorough evaluation of distortion correction performance in the context of submillimetre resolution and its potential

impact on fMRI analysis. To achieve this, various qualitative and quantitative evaluation criteria were proposed, including assessments of spatial resolution (σ_{deg}), co-registration accuracy (LPIPS index), functional mapping accuracy (r_{GM}), and functional distribution ($\rho_{HO,HC}$, D, and p-value).

One frequently addressed concern associated with distortion correction is the potential loss of spatial resolution arising from the unwarping process, which involves resampling or repositioning of voxels (Renvall et al., 2016; Kashyap et al., 2018). However, the analysis results demonstrate that the potential degradation in spatial resolution caused by the distortion-correction process was minimal, as confirmed by data from five subjects. This work employed ANTs to implement the blip-up-blip-down distortion correction. In the community, other software packages are also available for the same purpose, including 3DQwarp (AFNI) (https://afni.nimh.nih.gov), COPE (Brain Voyager) (https://www.brainvoyager.com), and TOPUP (FSL) (https://fsl.fmrib.ox.ac.uk/fsl), all of which have been employed in numerous previous submillimetre fMRI studies. In future work, the performance of these alternative distortion-correction software will be assessed in comparison to the ANTs, with the aim of determining the most optimal method for high-resolution fMRI.

Accurate mapping of detected neural signals onto the correct anatomical references requires precise co-registration between functional and anatomical scans, as measured by EPI and MP2RAGE. In particular, submillimetre fMRI, which allows for the characterisation of cortical depth-dependent functional activities, demands a clear definition of cortical regions, typically achieved using the structural information derived from the anatomical scan (Margalit et al., 2020; Jia et al., 2021; Deshpande et al., 2022). The distortion correction demonstrated here exhibited significant improvements in the co-registration between the EPI and MP2RAGE scans, as confirmed by both visual inspection as well as the quantitative

LPIPS index. However, the distortion-corrected EPI images still suffer from the susceptibility-induced signal loss, which can be seen in regions around the frontal lobe. This can be reduced by employing dedicated RF pulses, also known as tailored RF methods (Yip et al., 2006; Zheng et al., 2013), or utilising an EPI-readout shortening technique such as EPI with Keyhole (EPIK) (Shah and Zilles, 2003, 2004; Zaitsev et al., 2001), the use of which has been demonstrated in a number of fMRI studies (Yun et al., 2013, 2019; Yun and Shah, 2017) including those focused on delineating the cortical depth-dependent profiles (Yun et al., 2022; Pais-Roldán et al., 2023). In this study, the target functional area was the visual cortex, where the susceptibility-induced signal loss is expected to be minimal. This allowed the investigation of the effect of distortion correction on functional activation with little concern for the signal loss issue.

The improved co-registration directly contributed to enhancing the accuracy of functional mapping onto the GM. Here, the distortion correction did not significantly affect the distribution of functional activation, as verified by the histogram distribution and the statistical assessment using the KS test. In the distortion-corrected case, a significant increase in r_{GM} was observed when compared to that from the original, uncorrected data. Nevertheless, a fraction of the activated voxels still appeared in the non-GM regions, with an average $r_{Non\text{-}GM}$ of 11.42% across the five-subject data sets. Several possible factors contribute to the presence of non-GM activated voxels. One explanation is imperfect distortion correction and the subsequent errors in co-registration. Another potential cause is false positive activation induced by motion or physiological fluctuations, such as respiration or cardiac pulse (Birn et al., 2006; Bright et al., 2013). The impact of physiological noise can be controlled to some extent by simultaneously recording the physiological signals during fMRI and regressing them out from the fMRI time-series data (Birn et al., 2006). Another factor may be the superficial bias effect typically seen in the gradient-echo BOLD methods. Various

approaches have been proposed to reduce this effect, including the use of prior information on venous structures (Koopmans et al., 2010; Kay et al., 2019) or phase-data-based regression methods (Menon et al., 2002; Stanley et al., 2021). We anticipate that when our fMRI setting is further combined with the physiological-noise or the superficial-bias control methods, an even higher r_{GM} will be achieved.

A distortion-matched anatomical scan, the readout of which is performed using the same EPI sequence as for fMRI, can be used as an alternative to the distortion correction method (Chai et al., 2021; van der Zwaag et al., 2018). This anatomical scan exhibits distortions identical to the fMRI scan, ensuring errorless co-registration between the two scans. This approach makes the co-registration process more straightforward compared to the scenario involving two different sequence modalities (e.g. EPI and MP2RAGE) (Kashyap et al., 2018; Navarro et al., 2021). However, due to the distorted anatomical reference, its application can be limited for the analyses that rely on accurate anatomical information, such as the morphometric measurement of cortical thickness or the cortical surface-based atlasing (Polimeni et al., 2018, Yun et al., 2024). The distortion in this anatomical scan can also be corrected using the reversed PE method. In this case, the same simultaneous acquisition scheme proposed in this work can be effectively deployed to minimise the total acquisition time and energy accumulation.

One limitation of the reversed PE method is its relatively time-consuming process. In our fMRI data, which consists of 96 temporal volumes, each containing 9.7 M voxels (i.e. 288 × 288 × 117 slices), the processing time on a standalone PC (Intel Core i7-8850H CPU 2.60 GHz with 32GB RAM) was approximately 6.5 hours. The processor used here has a single socket and 12 parallel processing threads, which were fully exploited during the ANTs computation. However, given that our processor is relatively old (Intel Core 8th generation, released in Apr. 2018), the use of a more powerful processor with multiple sockets under a

workstation environment (e.g. eight sockets, 48 threads with Intel Xeon Processor E7, yielding 384 parallel processing threads), could drastically reduce the processing time, allowing for a timely reconstruction for entire submillimetre fMRI data with distortion correction.

In conclusion, this work presents a novel EPI scheme that simultaneously acquires reversed PE data in a single measurement, and its utility for submillimetre (0.73×0.73 mm^2) fMRI has been demonstrated at 7T. This strategy effectively spares another acquisition time and RF energy accumulation for the parallel imaging calibration scans, making the method particularly applicable for time-critical clinical applications. The performance of distortion correction was evaluated in direct comparison with original, uncorrected data using the various quantitative and qualitative assessment criteria proposed here. The results demonstrate improved functional mapping accuracy without significant degradation of spatial resolution or alternation of the functional activation distribution. This provides direct insight into the effectiveness of distortion correction for submillimetre fMRI, as demonstrated in this study.

5. Acknowledgement

The authors would like to thank the volunteers for their participation in this work and Claire Rick for English proofreading.

6. References

Aja-Fernandez, S., Martin, D. G., Tristan-Vega, A., & Vegas-Sanchez-Ferrero, G. (2015). Improving GRAPPA reconstruction by frequency discrimination in the ACS lines. Int J Comput Assist Radiol Surg, 10(10), 1699-1710. doi:10.1007/s11548-015-1172-7

Avants, B. B., Tustison, N. J., Song, G., Cook, P. A., Klein, A., & Gee, J. C. (2011). A reproducible evaluation of ANTs similarity metric performance in brain image registration. Neuroimage, 54(3), 2033-2044. doi:10.1016/j.neuroimage.2010.09.025

Balteau, E., Hutton, C., & Weiskopf, N. (2010). Improved shimming for fMRI specifically optimizing the local BOLD sensitivity. Neuroimage, 49(1), 327-336. doi:10.1016/j.neuroimage.2009.08.010

Birn, R. M., Diamond, J. B., Smith, M. A., & Bandettini, P. A. (2006). Separating respiratory-variation-related fluctuations from neuronal-activity-related fluctuations in fMRI. Neuroimage, 31(4), 1536-1548. doi:10.1016/j.neuroimage.2006.02.048

Bright, M. G., & Murphy, K. (2013). Removing motion and physiological artifacts from intrinsic BOLD fluctuations using short echo data. Neuroimage, 64(6), 526-537. doi:10.1016/j.neuroimage.2012.09.043

Chai, Y., Li, L., Wang, Y., Huber, L., Poser, B. A., Duyn, J., & Bandettini, P. A. (2021). Magnetization transfer weighted EPI facilitates cortical depth determination in native fMRI space. Neuroimage, 242, 118455. doi:10.1016/j.neuroimage.2021.118455

Chang, H., & Fitzpatrick, J. M. (1992). A technique for accurate magnetic resonance imaging in the presence of field inhomogeneities. IEEE Trans Med Imaging, 11(3), 319-329. doi:10.1109/42.158935

Chang, Y., Pham, H. A., & Li, Z. (2022). A dual-interpolator method for improving parallel MRI reconstruction. Magn Reson Imaging, 92, 108-119. doi:10.1016/j.mri.2022.06.009

Chen, N. K., & Wyrwicz, A. M. (1999). Correction for EPI distortions using multi-echo gradient-echo imaging. Magn Reson Med, 41(6), 1206-1213. doi:10.1002/(sici)1522-2594(199906)41:6<1206::aid-mrm17>3.0.co;2-l

Chung, J. Y., In, M. H., Oh, S. H., Zaitsev, M., Speck, O., & Cho, Z. H. (2011). An improved PSF mapping method for EPI distortion correction in human brain at ultra high field (7T). MAGMA, 24(3), 179-190. doi:10.1007/s10334-011-0251-1

Deshpande, G., Wang, Y., & Robinson, J. (2022). Resting state fMRI connectivity is sensitive to laminar connectional architecture in the human brain. Brain Inform, 9(1), 2. doi:10.1186/s40708-021-00150-4

Duong, S. T. M., Phung, S. L., Bouzerdoum, A., & Schira, M. M. (2020). An unsupervised deep learning technique for susceptibility artifact correction in reversed phase-encoding EPI images. Magn Reson Imaging, 71, 1-10. doi:10.1016/j.mri.2020.04.004

Dymerska, B., Poser, B. A., Barth, M., Trattnig, S., & Robinson, S. D. (2018). A method for the dynamic correction of B(0)-related distortions in single-echo EPI at 7T. Neuroimage, 168, 321-331. doi:10.1016/j.neuroimage.2016.07.009

Esteban, O., Markiewicz, C. J., Blair, R. W., Moodie, C. A., Isik, A. I., Erramuzpe, A., et al. (2019). fMRIPrep: a robust preprocessing pipeline for functional MRI. Nat Methods, 16(1), 111-116. doi:10.1038/s41592-018-0235-4

Glasser, M. F., Sotiropoulos, S. N., Wilson, J. A., Coalson, T. S., Fischl, B., Andersson, J. L., et al. (2013). The minimal preprocessing pipelines for the Human Connectome Project. Neuroimage, 80, 105-124. doi:10.1016/j.neuroimage.2013.04.127

Griswold, M. A., Jakob, P. M., Heidemann, R. M., Nittka, M., Jellus, V., Wang, J., et al. (2002). Generalized autocalibrating partially parallel acquisitions (GRAPPA). Magn Reson Med, 47(6), 1202-1210. doi:10.1002/mrm.10171

Holland, D., Kuperman, J. M., & Dale, A. M. (2010). Efficient correction of inhomogeneous static magnetic field-induced distortion in Echo Planar Imaging. Neuroimage, 50(1), 175-183. doi:10.1016/j.neuroimage.2009.11.044

Hong, X., To, X. V., Teh, I., Soh, J. R., & Chuang, K. H. (2015). Evaluation of EPI distortion correction methods for quantitative MRI of the brain at high magnetic field. Magn Reson Imaging, 33(9), 1098-1105. doi:10.1016/j.mri.2015.06.010

Huang, P., Correia, M. M., Rua, C., Rodgers, C. T., Henson, R. N., & Carlin, J. D. (2021). Correcting for Superficial Bias in 7T Gradient Echo fMRI. Front Neurosci, 15, 715549. doi:10.3389/fnins.2021.715549

Hutton, C., Bork, A., Josephs, O., Deichmann, R., Ashburner, J., & Turner, R. (2002). Image distortion correction in fMRI: A quantitative evaluation. Neuroimage, 16(1), 217-240. doi:10.1006/nimg.2001.1054

Jezzard, P., & Balaban, R. S. (1995). Correction for geometric distortion in echo planar images from B0 field variations. Magn Reson Med, 34(1), 65-73. doi:10.1002/mrm.1910340111

Jia, K., Zamboni, E., Kemper, V., Rua, C., Goncalves, N. R., Ng, A. K. T., et al. (2020). Recurrent Processing Drives Perceptual Plasticity. Curr Biol, 30(21), 4177-4187 e4174. doi:10.1016/j.cub.2020.08.016

Jia, K., Zamboni, E., Rua, C., Goncalves, N. R., Kemper, V., Ng, A. K. T., et al. (2021). A protocol for ultra-high field laminar fMRI in the human brain. STAR Protoc, 2(2), 100415. doi:10.1016/j.xpro.2021.100415

Kashyap, S., Ivanov, D., Havlicek, M., Poser, B. A., & Uludag, K. (2018). Impact of acquisition and analysis strategies on cortical depth-dependent fMRI. Neuroimage, 168, 332-344. doi:10.1016/j.neuroimage.2017.05.022

Kay, K., Jamison, K. W., Vizioli, L., Zhang, R., Margalit, E., & Ugurbil, K. (2019). A critical assessment of data quality and venous effects in sub-millimeter fMRI. Neuroimage, 189, 847-869. doi:10.1016/j.neuroimage.2019.02.006

Kim, T., Lee, Y., Zhao, T., Hetherington, H. P., & Pan, J. W. (2017). Gradient-echo EPI using a high-degree shim insert coil at 7 T: Implications for BOLD fMRI. Magn Reson Med, 78(5), 1734-1745. doi:10.1002/mrm.26563

Koopmans, P. J., Barth, M., & Norris, D. G. (2010). Layer-specific BOLD activation in human V1. Hum Brain Mapp, 31(9), 1297-1304. doi:10.1002/hbm.20936

Lohmann, G., Stelzer, J., Lacosse, E., Kumar, V. J., Mueller, K., Kuehn, E., et al. (2018). LISA improves statistical analysis for fMRI. Nat Commun, 9(1), 4014. doi:10.1038/s41467-018-06304-z

Malekian, V., Graedel, N. N., Hickling, A., Aghaeifar, A., Dymerska, B., Corbin, N., . . . Callaghan, M. F. (2023). Mitigating susceptibility-induced distortions in high-resolution 3DEPI fMRI at 7T. Neuroimage, 279, 120294. doi:10.1016/j.neuroimage.2023.120294

Mansfield, P. (1977). Multi-Planar Image-Formation Using Nmr Spin Echoes. Journal of Physics C-Solid State Physics, 10(3), L55-L58. doi:Doi 10.1088/0022-3719/10/3/004

Margalit, E., Jamison, K. W., Weiner, K. S., Vizioli, L., Zhang, R. Y., Kay, K. N., & Grill-Spector, K. (2020). Ultra-high-resolution fMRI of Human Ventral Temporal Cortex Reveals Differential Representation of Categories and Domains. J Neurosci, 40(15), 3008-3024. doi:10.1523/JNEUROSCI.2106-19.2020

Margosian, P. (1985). Faster MR. Imaing – Imaging with half the data. Proceedings of the 4th Annual Meeting of SMRM. International Society for Magnetic Resonance in Medicine, p 1024.

Marquardt, I., Schneider, M., Gulban, O. F., Ivanov, D., & Uludag, K. (2018). Cortical depth profiles of luminance contrast responses in human V1 and V2 using 7 T fMRI. Hum Brain Mapp, 39(7), 2812-2827. doi:10.1002/hbm.24042

Menon, R. S. (2002). Postacquisition suppression of large-vessel BOLD signals in high-resolution fMRI. Magn Reson Med, 47(1), 1-9. doi:10.1002/mrm.10041

Montez, D. F., Van, A. N., Miller, R. L., Seider, N. A., Marek, S., Zheng, A., et al. (2023). Using synthetic MR images for distortion correction. Dev Cogn Neurosci, 60, 101234. doi:10.1016/j.dcn.2023.101234

Morgan, P. S., Bowtell, R. W., McIntyre, D. J., & Worthington, B. S. (2004). Correction of spatial distortion in EPI due to inhomogeneous static magnetic fields using the reversed gradient method. J Magn Reson Imaging, 19(4), 499-507. doi:10.1002/jmri.20032

Navarro, K. T., Sanchez, M. J., Engel, S. A., Olman, C. A., & Weldon, K. B. (2021). Depth-dependent functional MRI responses to chromatic and achromatic stimuli throughout V1 and V2. Neuroimage, 226, 117520. doi:10.1016/j.neuroimage.2020.117520

Pais-Roldan, P., Yun, S. D., Palomero-Gallagher, N., & Shah, N. J. (2023). Cortical depth-dependent human fMRI of resting-state networks using EPIK. Front Neurosci, 17, 1151544. doi:10.3389/fnins.2023.1151544

Park, J., Zhang, Q., Jellus, V., Simonetti, O., & Li, D. (2005). Artifact and noise suppression in GRAPPA imaging using improved k-space coil calibration and variable density sampling. Magn Reson Med, 53(1), 186-193. doi:10.1002/mrm.20328

Patzig, F., Mildner, T., Schlumm, T., Muller, R., & Moller, H. E. (2021). Deconvolution-based distortion correction of EPI using analytic single-voxel point-spread functions. Magn Reson Med, 85(5), 2445-2461. doi:10.1002/mrm.28591

Polimeni, J. R., Renvall, V., Zaretskaya, N., & Fischl, B. (2018). Analysis strategies for high-resolution UHF-fMRI data. Neuroimage, 168, 296-320. doi:10.1016/j.neuroimage.2017.04.053

Renvall, V., Witzel, T., Wald, L. L., & Polimeni, J. R. (2016). Automatic cortical surface reconstruction of high-resolution T1 echo planar imaging data. Neuroimage, 134, 338-354. doi:10.1016/j.neuroimage.2016.04.004

Robson, M. D., Gore, J. C., & Constable, R. T. (1997). Measurement of the point spread function in MRI using constant time imaging. Magn Reson Med, 38(5), 733-740. doi:10.1002/mrm.1910380509

Schellekens, W., Bhogal, A. A., Roefs, E. C., Baez-Yanez, M. G., Siero, J. C., & Petridou, N. (2023). The many layers of BOLD. The effect of hypercapnic and hyperoxic stimuli on macro- and micro-vascular compartments quantified by CVR, M, and CBV across cortical depth. J Cereb Blood Flow Metab, 43(3), 419-432. doi:10.1177/0271678X221133972

Shah, N. J., & Zilles, K. (2003). Verfahren zur Untersuchung eines Objekts mittels Erfassung des Ortsfrequenzraumes. DE 000019962845 C2.

Shah, N. J., & Zilles, K. (2004). Imaging process in the spatial frequency space and useful for examining the properties of object. US 6781372 B2.

Sheng, J., Shi, Y., & Zhang, Q. (2021). Improved parallel magnetic resonance imaging reconstruction with multiple variable density sampling. Sci Rep, 11(1), 9005. doi:10.1038/s41598-021-88567-z

Stanley, O. W., Kuurstra, A. B., Klassen, L. M., Menon, R. S., & Gati, J. S. (2021). Effects of phase regression on high-resolution functional MRI of the primary visual cortex. Neuroimage, 227, 117631. doi:10.1016/j.neuroimage.2020.117631

Tustison, N. J., Cook, P. A., Holbrook, A. J., Johnson, H. J., Muschelli, J., Devenyi, G. A., et al. (2021). The ANTsX ecosystem for quantitative biological and medical imaging. Sci Rep, 11(1), 9068. doi:10.1038/s41598-021-87564-6

van der Zwaag, W., Buur, P. F., Fracasso, A., van Doesum, T., Uludag, K., Versluis, M. J., & Marques, J. P. (2018). Distortion-matched T(1) maps and unbiased T(1)-weighted images as anatomical reference for high-resolution fMRI. Neuroimage, 176, 41-55. doi:10.1016/j.neuroimage.2018.04.026

Wang, J., Nasr, S., Roe, A. W., & Polimeni, J. R. (2022). Critical factors in achieving fine-scale functional MRI: Removing sources of inadvertent spatial smoothing. Hum Brain Mapp, 43(11), 3311-3331. doi:10.1002/hbm.25867

Wang, S., Peterson, D. J., Gatenby, J. C., Li, W., Grabowski, T. J., & Madhyastha, T. M. (2017). Evaluation of Field Map and Nonlinear Registration Methods for Correction of Susceptibility Artifacts in Diffusion MRI. Front Neuroinform, 11, 17. doi:10.3389/fninf.2017.00017

Wang, X., Wang, H., & Zhou, J. (2014). Improve GRAPPA with cross-sampled ACS lines and nonlinear kernel model. Biomed Mater Eng, 24(1), 1101-1108. doi:10.3233/BME-130909

Yip, C. Y., Fessler, J. A., & Noll, D. C. (2006). Advanced three-dimensional tailored RF pulse for signal recovery in T2*-weighted functional magnetic resonance imaging. Magn Reson Med, 56(5), 1050-1059. doi:10.1002/mrm.21048

Yun, S. D., Kuppers, F., & Shah, N. J. (2023a). Submillimeter fMRI Acquisition Techniques for Detection of Laminar and Columnar Level Brain Activation. J Magn Reson Imaging. doi:10.1002/jmri.28911

Yun, S. D., Pais-Roldan, P., Palomero-Gallagher, N., & Shah, N. J. (2022). Mapping of whole-cerebrum resting-state networks using ultra-high resolution acquisition protocols. Hum Brain Mapp, 43(11), 3386-3403. doi:10.1002/hbm.25855

Yun, S. D., Reske, M., Vahedipour, K., Warbrick, T., & Shah, N. J. (2013). Parallel imaging acceleration of EPIK for reduced image distortions in fMRI. Neuroimage, 73, 135-143. doi:10.1016/j.neuroimage.2013.01.070

Yun, S. D., & Shah, N. J. (2017). Whole-brain high in-plane resolution fMRI using accelerated EPIK for enhanced characterisation of functional areas at 3T. PLoS One, 12(9), e0184759. doi:10.1371/journal.pone.0184759

Yun, S. D., & Shah, N. J. (2023b). A simultaneous measurement of opposite-phase-encoding EPI in a single fMRI session for the reduction of acquisition time and SAR at 7T. Proceedings of the 32nd Annual Meeting of ISMRM. International Society for Magnetic Resonance in Medicine, Toronto, Abstract 1161.

Yun, S. D., Weidner, R., Weiss, P. H., & Shah, N. J. (2019). Evaluating the Utility of EPIK in a Finger Tapping fMRI Experiment using BOLD Detection and Effective Connectivity. Sci Rep, 9(1), 10978. doi:10.1038/s41598-019-47341-y

Zaitsev, M., Hennig, J., & Speck, O. (2004). Point spread function mapping with parallel imaging techniques and high acceleration factors: fast, robust, and flexible method for echo-planar imaging distortion correction. Magn Reson Med, 52(5), 1156-1166. doi:10.1002/mrm.20261

Zaitsev, M., Zilles, K., & Shah, N. J. (2001). Shared k-space echo planar imaging with keyhole. Magn Reson Med, 45(1), 109-117. doi:10.1002/1522-2594(200101)45:1<109::aid-mrm1015>3.0.co;2-x

Zeng, H., & Constable, R. T. (2002). Image distortion correction in EPI: comparison of field mapping with point spread function mapping. Magn Reson Med, 48(1), 137-146. doi:10.1002/mrm.10200

Zheng, H., Zhao, T., Qian, Y., Schirda, C., Ibrahim, T. S., & Boada, F. E. (2013). Multi-slice parallel transmission three-dimensional tailored RF (PTX 3DTRF) pulse design for signal recovery in ultra high field functional MRI. J Magn Reson, 228, 37-44. doi:10.1016/j.jmr.2012.12.021

Declaration of interests

The authors declare no competing interests.

Funding sources

S.Y. and J. L. were supported by the National Research Foundation of Korea (NRF) grant funded by the Korean government (Ministry of Science and ICT)(No. RS-2023-00254343). E.G. acknowledges support from the Deutsche Forschungsgemeinschaft (DFG) SFB 1280 projects A03 and F02 (project number: 316803389). The funders had no role in the study design, data collection and analysis, decision to publish, or preparation of the manuscript. None of the other authors receive any specific grant from funding agencies in the public, commercial, or not-for-profit sectors.

Declaration of generative AI in scientific writing

During the preparation of this work, the author used ChatGPT-3.5 (free version) solely to enhance the readability and language of the manuscript. The initial text was carefully written by the authors, and after receiving ChatGPT's suggestions, the author reviewed and edited the content as needed. No paragraphs were originally generated by AI. The authors take full responsibility for the content of the published article

Author Contributions

S. Y. designed the research; S.Y. developed the proposed MR imaging sequence and the corresponding image reconstruction software; S.Y. performed data acquisition and analysis; S.Y. wrote the draft of the manuscript and revised it; E.G. introduced the geometric distortion using the ANTs software, and reviewed the manuscript. J. L. performed data acquisition and analysis, and reviewed the manuscript. N.J.S. and S.Y held critical discussions; N.J.S. reviewed and revised the manuscript; N.J.S supported the maintenance and use of the 7T MRI scanner.

Tables

Table 1. Lookup table showing the SD values of the original image, smoothed with a range of kernel widths (σ), at the specified slice location (see Fig. 4). The SD of distortion-correction image was computed as 72.55, which is closest to the original image with no smoothing applied (i.e. first column).

σ (mm)	**0.0**	**0.2**	**0.3**	**0.4**	**0.5**	**0.6**	**0.7**	**0.8**
SD	72.76	70.76	69.97	69.26	68.66	68.15	67.69	68.66

Table 2. Structural similarity between EPI and MP2RAGE (LPIPS index). On average, the distortion-corrected EPI showed a substantial reduction in the LPIPS index compared to the original EPI, with decreases of 7.85%, 5.03%, and 7.83% for GM, WM, and CSF, respectively.

Subject	**Original EPI**			**Distortion-corrected EPI**		
	GM	**WM**	**CSF**	**GM**	**WM**	**CSF**
1	0.187	0.159	0.153	0.167	0.145	0.142
2	0.183	0.152	0.170	0.174	0.145	0.162
3	0.186	0.159	0.151	0.177	0.152	0.143
4	0.218	0.176	0.195	0.194	0.172	0.177
5	0.179	0.148	0.162	0.167	0.145	0.142
Average	0.191	0.159	0.166	0.176	0.151	0.153

Table 3. The ratio of activated voxels located in the GM and non-GM regions (r_{GM} and $r_{Non\text{-}GM}$). The results from distortion-corrected EPI show substantial increases in r_{GM} (88.58 ± 2.51%) when compared to that from original, uncorrected EPI (80.25 ± 1.69%).

Subject	**Original EPI**		**Distortion-corrected EPI**	
	r_{GM} **(%)**	$r_{Non\text{-}GM}$ **(%)**	r_{GM} **(%)**	$r_{Non\text{-}GM}$ **(%)**
1	78.96	21.04	88.86	11.14
2	78.50	21.50	86.43	13.57
3	82.78	17.22	89.09	10.91
4	80.73	19.27	86.16	13.84
5	80.30	19.70	92.38	7.62
mean ± SD	80.25 ± 1.69	19.75 ± 1.69	88.58 ± 2.51	11.42 ± 2.51

Table 4. Results of statistical measures used to evaluate the difference between the two functional distributions before and after distortion correction.

Subject	Correlation coefficient ($\rho_{HO,HC}$)	KS test (*D* and *p*-value)	
1	0.9990	0.0079	0.6819
2	0.9992	0.0094	0.0687
3	0.9996	0.0075	0.1941
4	0.9994	0.0059	0.2637
5	0.9996	0.0090	0.8211

Figure legend

Figure 1. Schematic diagram of an fMRI acquisition sequence. (**a**) Standard EPI and (**b**) proposed EPI. In the standard scheme, the reversed PE data are acquired in a separate session, requiring repeated measurements for the calibration scan. In contrast, the proposed scheme acquires the reversed PE data during the same session at the dummy stage, allowing the same calibration scan to be used for image reconstruction of both original and reversed-PE data. The blue and red arrows denote the original and reversed PE directions, respectively. In this work, the number of dummy and reversed PE scans was configured to four and two, as illustrated in the figure.

Figure 2. Reconstructed images at four representative slice locations. The first and second rows display images obtained from the reversed and original PE directions. The last row shows the corresponding distortion-corrected results, revealing no significant visible loss of spatial resolution.

Figure 3. Effects of subject motion on distortion correction. (**a**) Reversed PE images obtained using the standard (left) and proposed (right) schemes. (**b**) Ventricle boundaries extracted from both images in Fig. a, shown in yellow (standard) and magenta (proposed), overlaid on the reversed PE image from the proposed method, illustrating significant motion displacement between the two cases. (**c**) Corresponding distortion-corrected images generated from the reversed PE images in Fig. a. (**d**) Original, uncorrected EPI image. (**e**) Enlarged depiction of the rectangular ROIs, highlighting effective distortion correction for both the standard and proposed schemes. However, the proposed scheme demonstrates greater

improvement in signal recovery and delineation of GM and WM boundaries around the frontal lobe (see arrows).

Figure 4. Results of spatial resolution assessments. (**a**) Original and distortion-corrected EPI images at a representative slice with selected ROIs: yellow for SD computation, and white (original) and green (distortion-corrected) for visual inspection. (**b**) From top-left to bottom-right, enlarged depictions of the rectangular ROIs are shown for the following: original EPI, original EPI smoothed with Gaussian kernel widths (σ) of 0.2, 0.4, 0.6 and 0.8, and distortion-corrected EPI. Visual inspection of image panel b suggests that the loss of spatial resolution in the distortion-corrected image is not significant.

Figure 5. Box-plot of the spatial resolution degradation (σ_{deg}) across five subjects. The results indicate that the spatial resolution degradation caused by distortion correction was not significant.

Figure 6. Results of co-registration to the anatomical scan (MP2RAGE). (**a**) Original EPI, (**b**) distortion-corrected EPI and (**c**) both results overlaid onto the MP2RAGE. In image panels a and b, the EPI and MP2RAGE scans are displayed alongside, each depicting the counterpart of the brain. The results from distortion-corrected EPI show improved alignment with the MP2RAGE scan, particularly around the regions marked by yellow boundaries (i.e. lateral and fourth ventricles) and red arrows; the boundary between the cingulate gyrus and corpus callosum is also shown to be well aligned. The overlapped depiction in image panel c further confirms the improved co-registration, where the ventricle signals are represented in red-yellow for the original EPI and blue-light blue for the corrected EPI.

Figure 7. Results of first-level analysis for visual fMRI (uncorrected $p < 0.001$). (**a**) The original (denoted in red-white) and distortion-corrected (denoted in cyan-magenta) results are overlaid on the co-registered MP2RAGE scan, revealing substantial differences in the localisation of activated voxels at the selected slice locations. A separate representation of the (**b**) original and (**c**) distortion-corrected results with the GM contour (denoted in white) further demonstrates that the activated voxels are more precisely localised along the cortical ribbon in the distortion-corrected case; see the enlarged depiction of the selected ROIs (see yellow arrows).

Figure 8. Analysis of histogram distribution from five subjects. For each subject, the histogram distribution of t-values obtained from the original (denoted in blue) and distortion-corrected (denoted in orange) fMRI data sets are depicted on the same plot, with the computed Pearson correlation coefficient. The histogram distribution and correlation values ($\rho > 0.99$ for all subjects) show a high degree of similarity, implying that the impact of distortion correction on the overall distribution of functional activation was not significant.

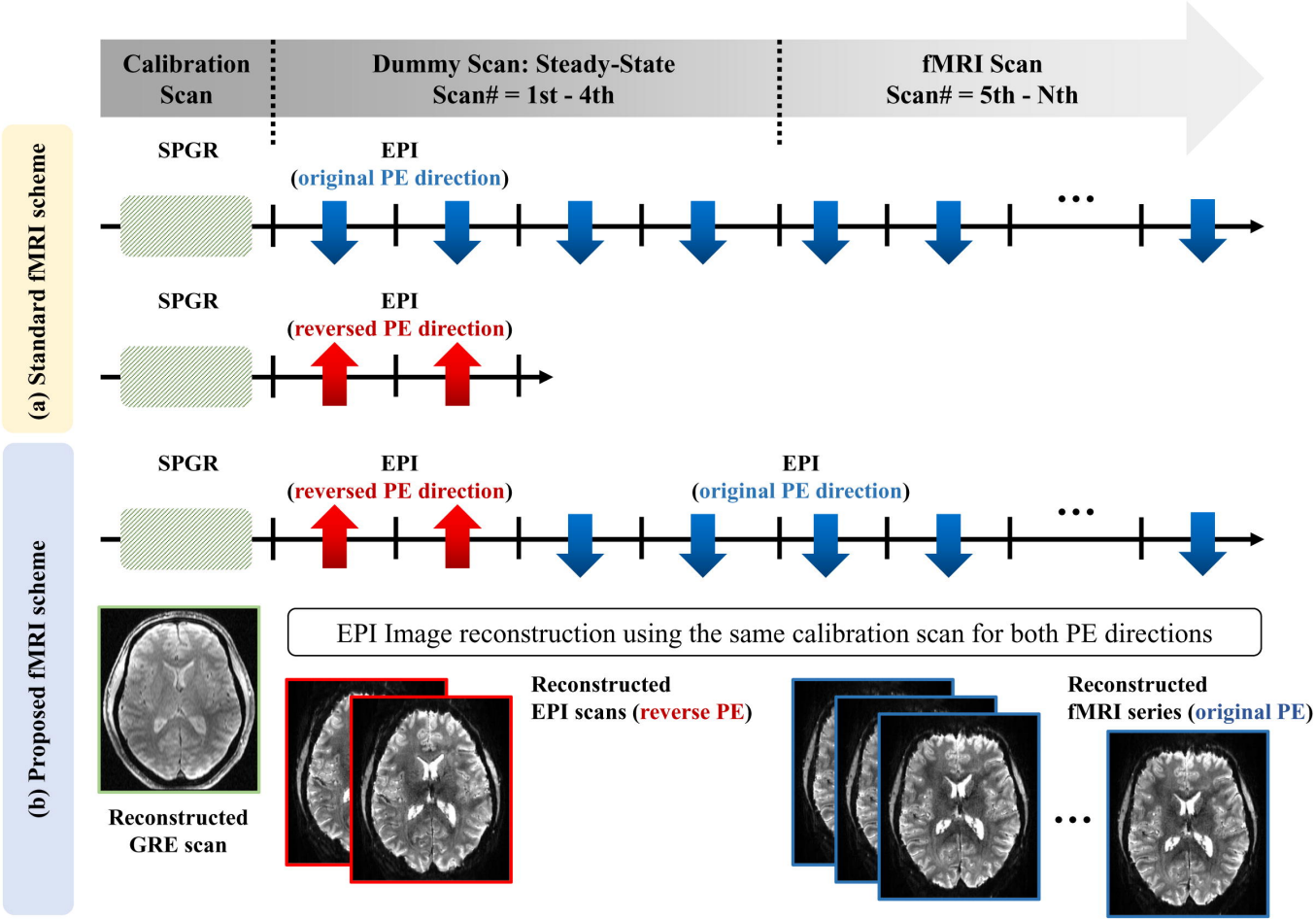
Calibration Scan
Dummy Scan: Steady-State
Scan# = 1st - 4th
fMRI Scan
Scan# = 5th - Nth
(a) Standard fMRI scheme
SPGR
EPI
(original PE direction)
SPGR
EPI
(reversed PE direction)
(b) Proposed fMRI scheme
SPGR
EPI
(reversed PE direction)
EPI
(original PE direction)
EPI Image reconstruction using the same calibration scan for both PE directions
Reconstructed GRE scan
Reconstructed EPI scans (reverse PE)
Reconstructed fMRI series (original PE)

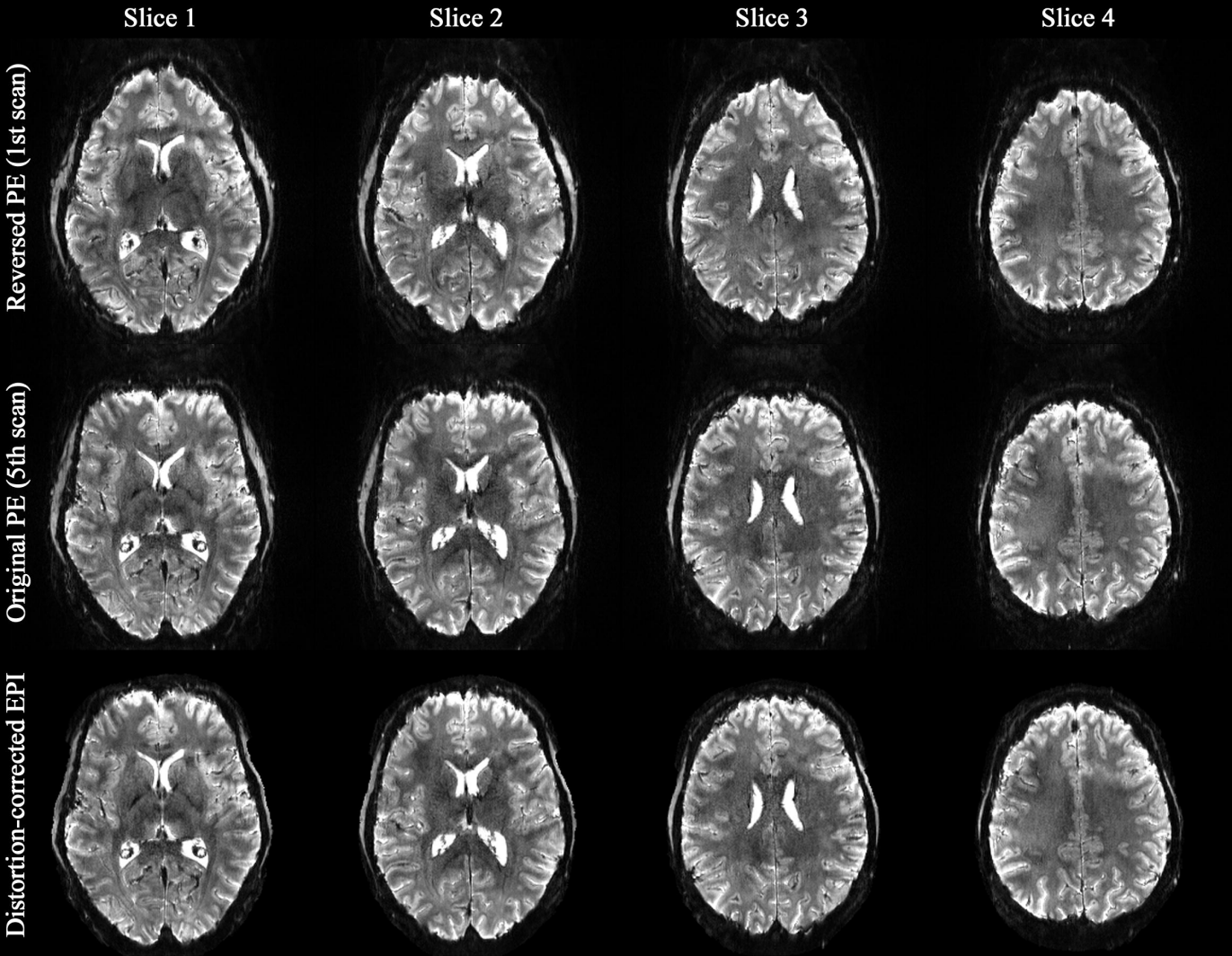
Slice 1
Slice 2
Slice 3
Slice 4
Reversed PE (1st scan)
Original PE (5th scan)
Distortion-corrected EPI

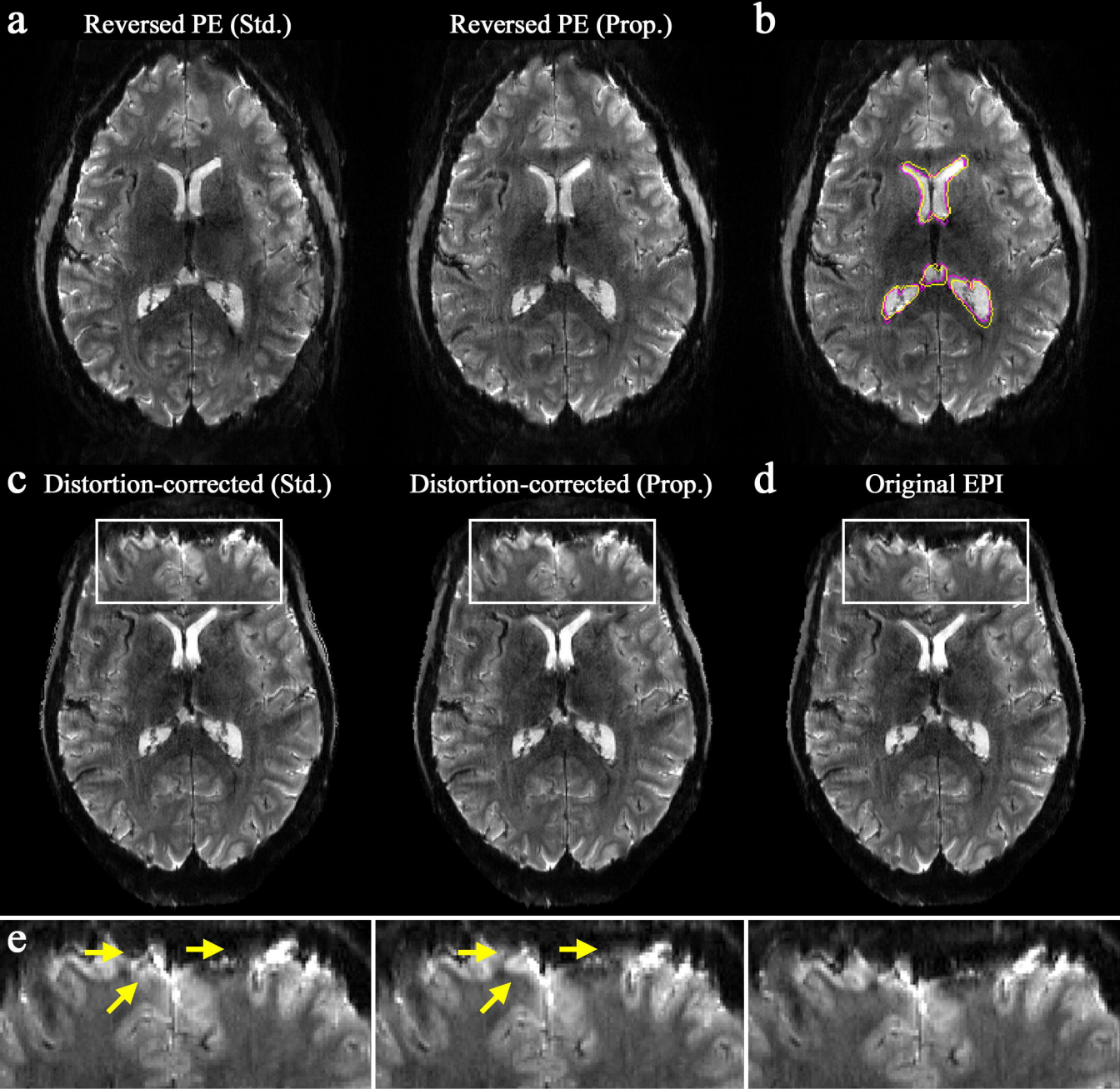
a
Reversed PE (Std.)
Reversed PE (Prop.)
b
c
Distortion-corrected (Std.)
Distortion-corrected (Prop.)
d
Original EPI
e

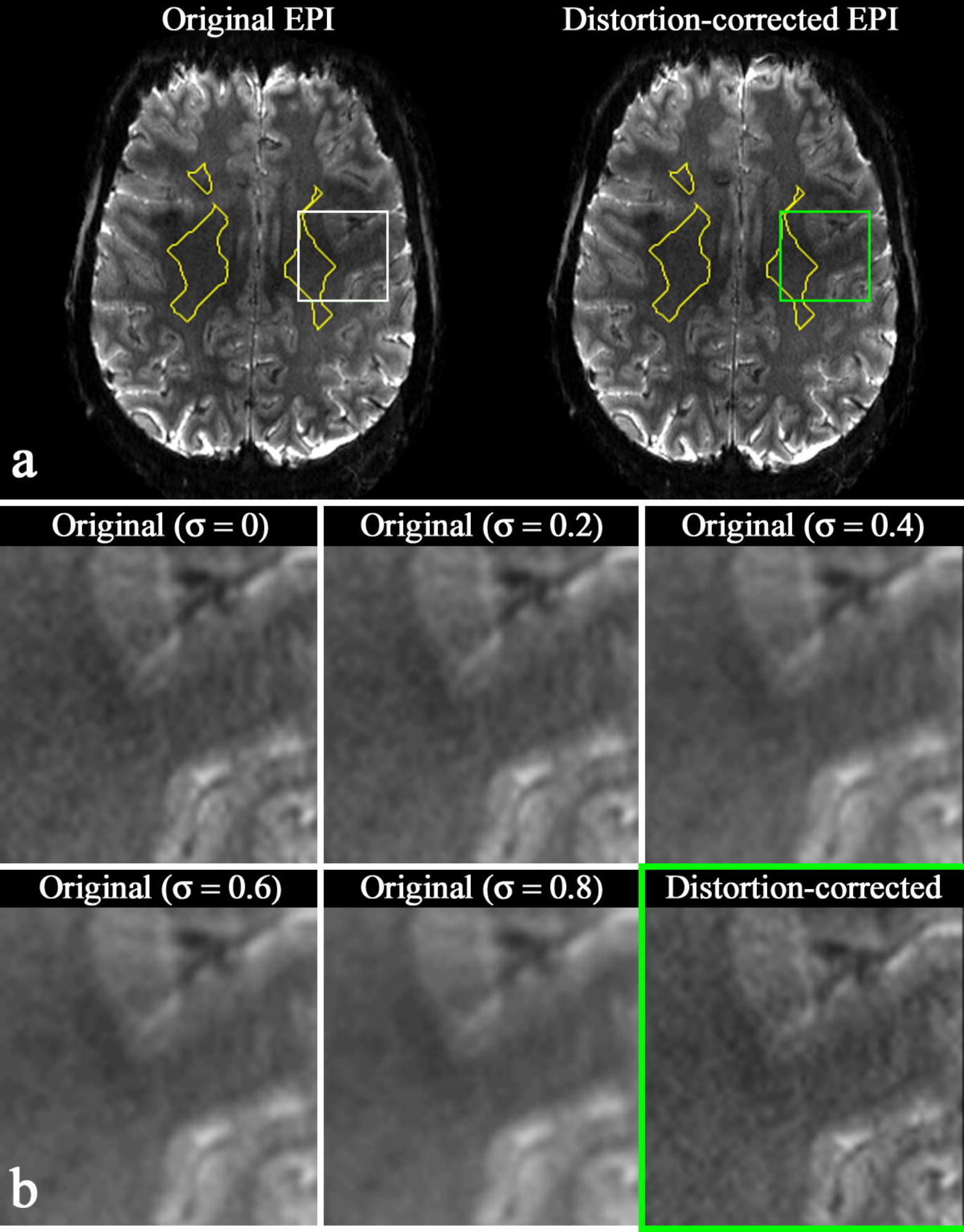
Original EPI
Distortion-corrected EPI
a
Original (σ = 0)
Original (σ = 0.2)
Original (σ = 0.4)
Original (σ = 0.6)
Original (σ = 0.8)
Distortion-corrected
b

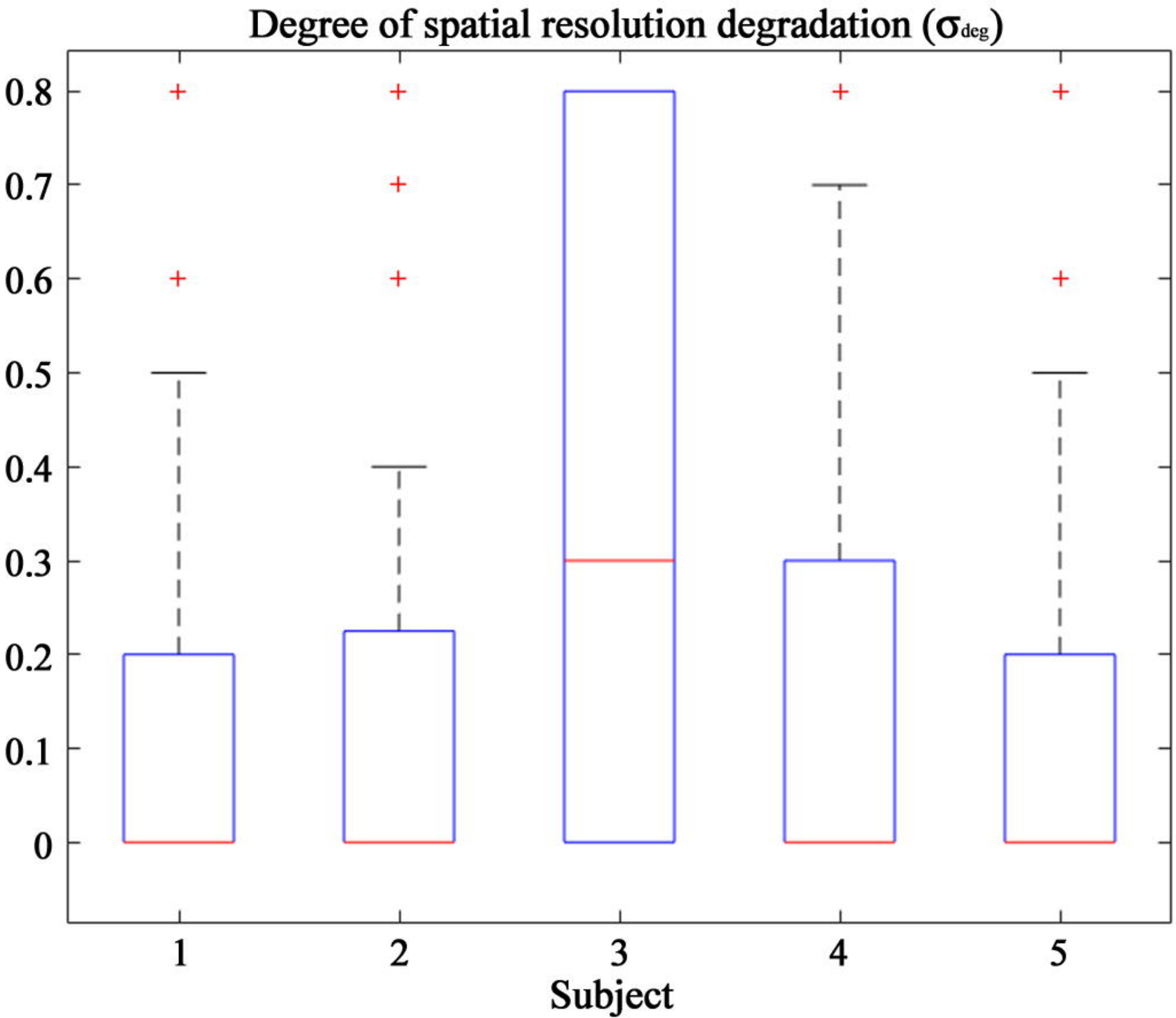
Degree of spatial resolution degradation (σ_{deg})
0.8
0.7
0.6
0.5
0.4
0.3
0.2
0.1
0
1
2
3
4
5
Subject

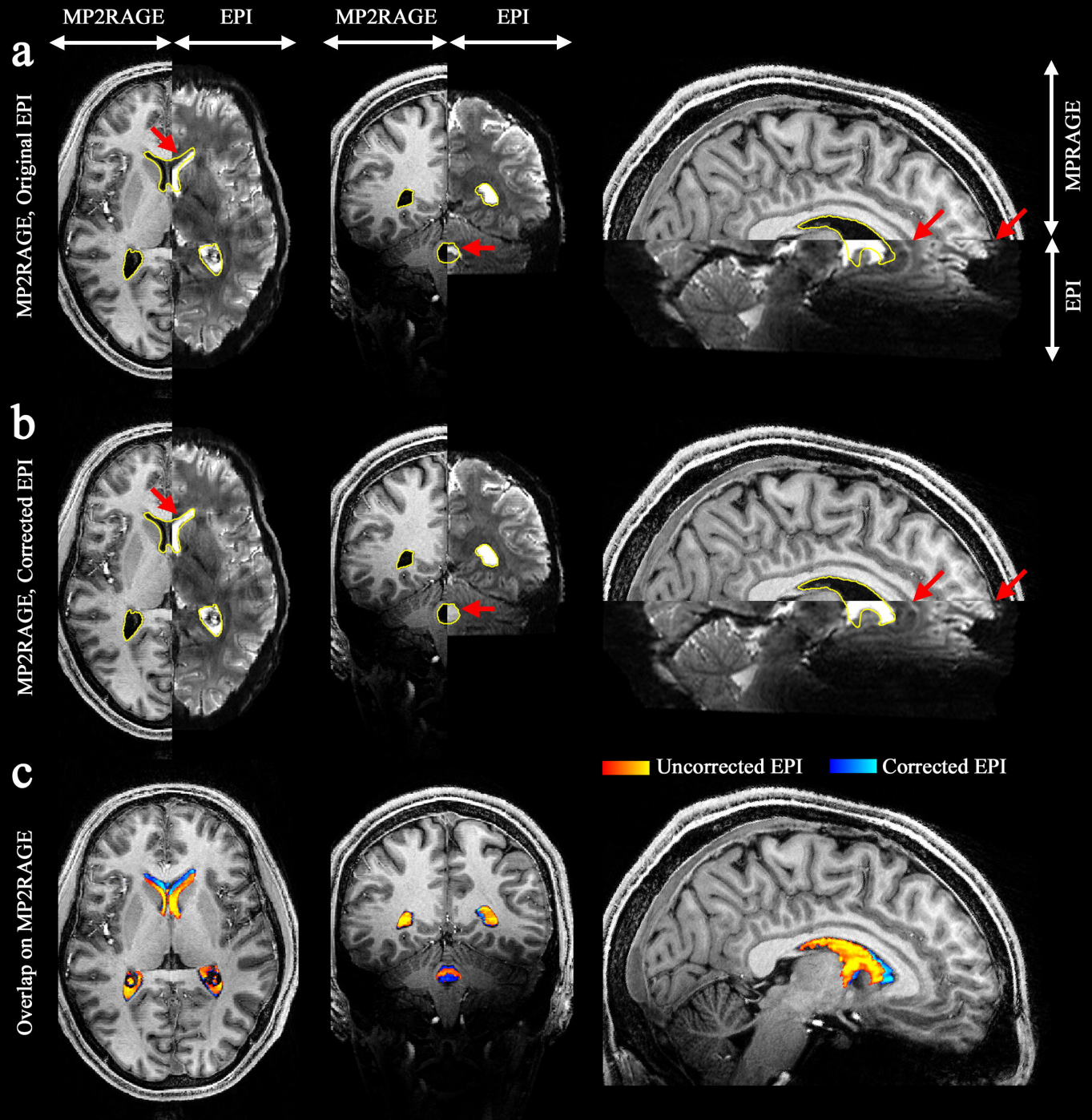
MP2RAGE
EPI
MP2RAGE
EPI
a
MP2RAGE, Original EPI
MPRAGE
EPI
b
MP2RAGE, Corrected EPI
c
Overlap on MP2RAGE
Uncorrected EPI
Corrected EPI

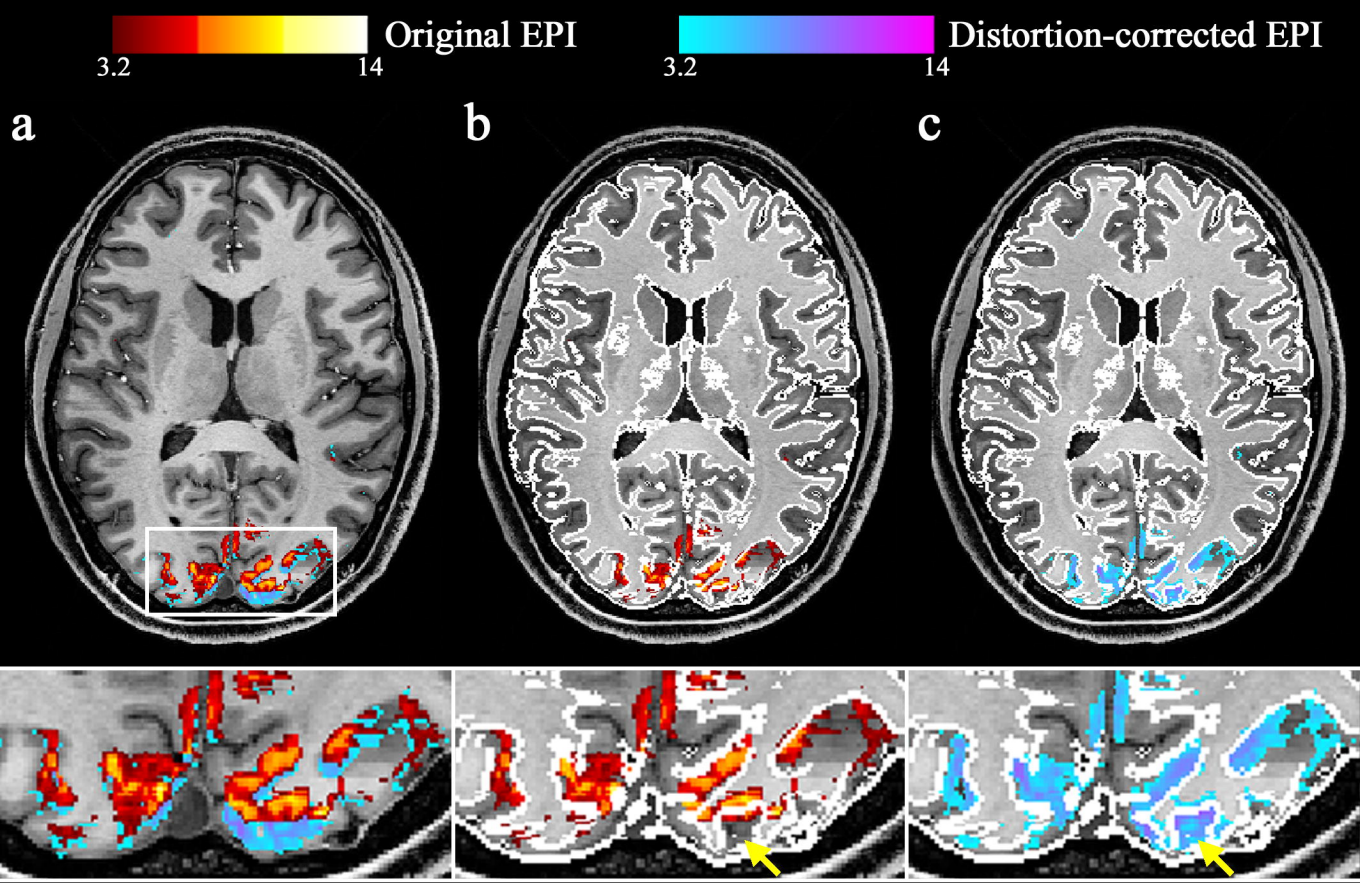
Original EPI
3.2
14
Distortion-corrected EPI
3.2
14
a
b
c

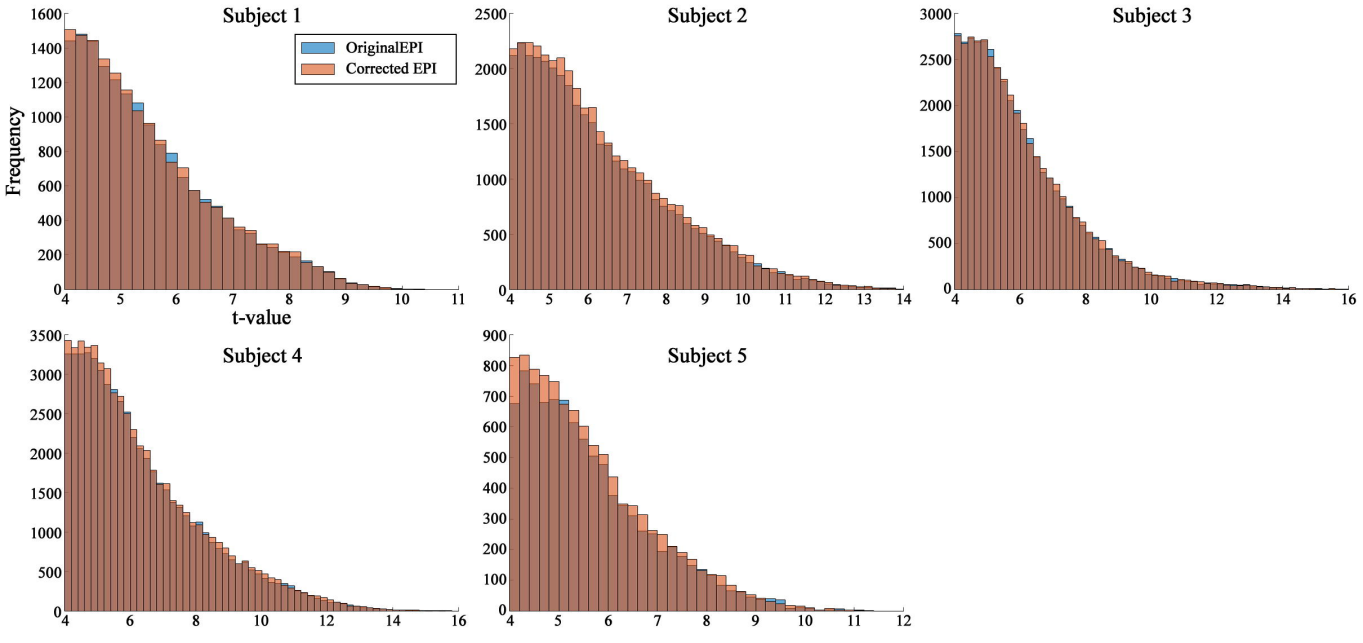
Subject 1
Subject 2
Subject 3
Subject 4
Subject 5
OriginalEPI
Corrected EPI
Frequency
t-value